JOURNAL OF GEOPHYSICAL RESEARCH, VOL. 105, NO. A8, PAGES 18,505–18,518, AUGUST 1, 2000

Large-scale vortex dynamics in the evening and midnight auroral zone: Observations and simulations

I. Voronkov

Department of Physics, University of Alberta, Edmonton, Alberta, Canada

E. F. Donovan and B. J. Jackel

Department of Physics and Astronomy, University of Calgary, Calgary, Alberta, Canada

J. C. Samson

Department of Physics, University of Alberta, Edmonton, Alberta, Canada

Abstract. We use Canadian Auroral Network for the OPEN Program Unified Study All-Sky Imager (ASI) and Meridional Scanning Photometer (MSP) data as the basis for a study of the dynamics of large-scale (hundreds of kilometers) auroral vortices. We consider 28 events corresponding to a range of auroral activity levels. Three of these are presented in detail, one corresponding to growth phase, one to pseudo-breakup and one to expansive phase onset. We show that vortex formation starts from a discrete arc with half thickness δ of the order of 20 km. This arc intensifies near the poleward boundary of enhanced proton aurora, as seen in the Hydrogen β (Hβ) MSP data and becomes azimuthally structured. This structuring is in the form of vortices with wavelength of the order of $\sim 2\pi\delta$. The vortices intensify and extend radially, leading to broadening of the initial arc. While the sizes and growth rates of the vortices vary, the overall scenario of vortex evolution is similar for all of the events. Structures that develop during the growth phase saturate at latitudes matching the poleward boundary of Hβ emissions and pseudo-breakup structures saturate further poleward. Expansive phase onset vortices expand poleward in a similar fashion, but we do not observe any saturation stage, presumably due to limitations imposed by the ASI field of view. We present results of shear flow ballooning vortex modeling in which we used initial conditions and parameters consistent with our observations. On the basis of our model results, we speculate that all of these experimentally observed vortices are the result of shear flow ballooning instability in the hot proton region in the near-Earth plasma sheet.

1. Introduction

Many studies of the magnetosphere-ionosphere interaction in the auroral region show that some intense energy releases from the magnetosphere to the ionosphere are accompanied by the appearance and intensification of large-scale (hundreds of kilometers) vortical structures that are seen as red and green images in the night sky. Intensification and subsequent evolution of auroral surge-like structures have historically been considered as important signature of the substorm expansive phase commencement [*Akasofu,* 1977]. Recent observations indicate that the evening and premidnight sectors appear to be most active with respect to large-scale vortex formation [*Steen and Collis,* 1988; *Kidd and Rostoker,* 1991; *Elphinstone et al.,* 1995; *Murphree and Johnson,* 1996; *Samson et al.,* 1996, 1998; *Frank et al.,* 1998] and that a vortex that is associated with substorm intensification appears at the equatorward edge of the auroral oval [*Frank et al.,* 1998]. Formation of such intense structures occurs at virtually the same time as other signatures of the beginning of the substorm expansive phase such as explosive growth of electron and proton precipitation, poleward motion of the proton precipitation region, and growth of Pi1 and Pi2 magnetic pulsations. This stimulates further study of large-scale vortex dynamics as a possible clue for understanding substorm intensification mechanisms.

Some studies have suggested that shear flow (or Kelvin-Helmholtz (KH)) instabilities due to velocity shears near auroral arcs can be responsible for the vortex formation [*Kelley,* 1986; *Kidd and Rostoker,* 1991; *Rankin et al.,* 1993; *Miura,* 1996; *Voronkov et al.,* 1999]. Apparently, however, the KH instability does not pro-

Paper number 1999JA000442.
0148-0227/00/1999JA000442$09.00

vide sufficient energy for the spatial extent and magnitudes observed for large-scale vortices [*Voronkov et al.*, 1999]. *Samson et al.* [1992] noted that some auroral intensifications start in the region of strong Hβ emissions and suggested that a possible energy source of the necessary potential energy is a high-energy proton region in the near-Earth plasma sheet. This idea is in agreement with direct measurements of the proton energy and plasma pressure at 8-10 Earth radii (R_E) in the midnight magnctotail [*Kistler et al.*, 1992]. Following this idea, *Voronkov et al.* [1997] presented a numerical model of possible interaction between shear flow and ballooning modes that potentially can appear in the region where the proton pressure gradient is in equilibrium with magnetic curvature forces. This interaction results in the fast-growing hybrid shear flow ballooning mode that extracts potential energy from the region and therefore grows to larger spatial extent and higher amplitudes than the KH mode.

Our objective is to trace dynamics of the large scale auroral vortices using data from the Canadian Auroral Network for the OPEN Program Unified Study (CANOPUS) All-Sky Imager (ASI) and Meridional Scanning Photometer (MSP) located in Gillam, Canada, and to compare these dynamics with results of numerical modeling for the shear flow ballooning instability. We begin with a description of the CANOPUS ASI and MSP and the data that we use in this study and present images and spatial and temporal characteristics for vortex dynamics (section 2). After that we describe our numerical model and present results of vortex simulations using parameters consistent with our interpretation of the data (section 3). In section 4 we discuss our simulation results within the context of the CANOPUS observations. Finally, in section 5 we summarize the results of this paper.

2. Observations

The CANOPUS project has supported the operation of an ASI and an MSP at Gillam, Canada, for over 10 years. In this study we use data from the Gillam ASI and MSP obtained during the years 1993 through 1996. Gillam is located at 56.4°N 265.4°E geodetic (GEOD). The Polar Anglo-American Conjugate Experiment (PACE) [*Baker and Wing*, 1989] latitude of the Gillam station is 67.4°, which corresponds to an L shell value of 6.7. Local midnight at Gillam occurs at roughly 0630 UT.

The ASI data we use consist of 557.7-nm images that were taken at 1-min intervals with an integration time of ~1.5 s. Assuming that the 557.7-nm emission originates at 110 km of altitude, the Gillam ASI provides a field of view from 54.5° to 59.3° geodetic latitudes and from 260.2° to 268.9° geodetic longitudes. The optical image intensity is sampled with 236 by 236 grid points. In this paper, we present all-sky images with geodetic coordinate grid lines plotted with 0.5° intervals, which corresponds to 56.6 km in the north-south direction and 31 km in the east-west direction at 110 km altitude. The central cross indicates geodetic latitude and longitude of the Gillam ASI. Magnetic north is shown by arrows.

The MSP data set consists of 1-min meridian scans of 486.1-nm (Hβ), 557.7-nm, and 630.0-nm optical emissions. One MSP scan provides intensities at 17 elevation angles. If the emissions originate at 110 km (which is a reasonable estimate for 486.1-nm and 557.7-nm emissions) then the scan gives a profile of emissions approximately along a magnetic meridian from ~63° to ~71° PACE (52°-60° geodetic) latitude with a resolution of roughly 0.5 degrees latitude. For emissions from 230 km (reasonable for the 630.0-nm emissions), the profile is along a magnetic meridian from ~60° to ~74° PACE (49°-63° GEOD) latitude with a resolution of roughly 1° latitude.

An extensive survey has resulted in the identification of near 400 north-south aligned auroral structures in the CANOPUS ASI data set [E. F. Donovan et al., North-south aligned auroral structures observed by an all-sky imager, submitted to *Geophysical Research Letters*, 2000]. The results of that study indicate that the probability of observing north-south structures in the aurora peaks near local midnight and that the probability distribution is narrower in local time than that for the observation of east-west aligned auroral arcs. This suggests that the occurrence of radial structures in the aurora is related to midnight auroral activity and substorm intensifications. Large-scale vortices were seen in conjunction with many of the north-south structures. We chose 28 events associated with large-scale vortices that had relatively slow growth rates and whose growth could therefore be studied using the 1-min ASI data. Below we present three events, one of which occurred during a substorm growth phase, one during a pseudobreakup, and one during an expansive phase onset.

The first event we would like to consider in this section relates to the vortex formation and its dynamics at 0206-0245 UT on March 29, 1995. This time interval corresponded to a substorm growth phase with an expansive phase onset at 0314 UT. The timing of the substorm intensification was made using the 557.7-nm green line and 630.0-nm red line emission magnitudes registered by the Gillam MSP. For this event the maximum of 557.7-nm intensity rose from 6559 R (corresponding to the background level during the growth phase) at 0314 UT to 32,039 R at 0315 UT, and further to 52,837 R at 0316 UT. The 630.0-nm intensity magnitude increased from 1257 R at 0314 UT to 2187 R at 0316 UT.

The Gillam MSP data for 486.1- and 630.0-nm emissions are presented in Figure 1. Figure 1a shows the meridional distribution of the Hβ (486.1 nm) emission which corresponds to the proton precipitation region [*Samson et al.*, 1992], and Figure 1b shows the red 630.0-nm emission which allows us to identify the region of auroral electron precipitation [*Blanchard et al.*, 1997] and field lines mapping to the electron plasma sheet. Figure 2 represents a sequence of all-sky images for this event and Figure 3 shows the magnitude of the ASI image intensity. For Figure 2 we have selected only

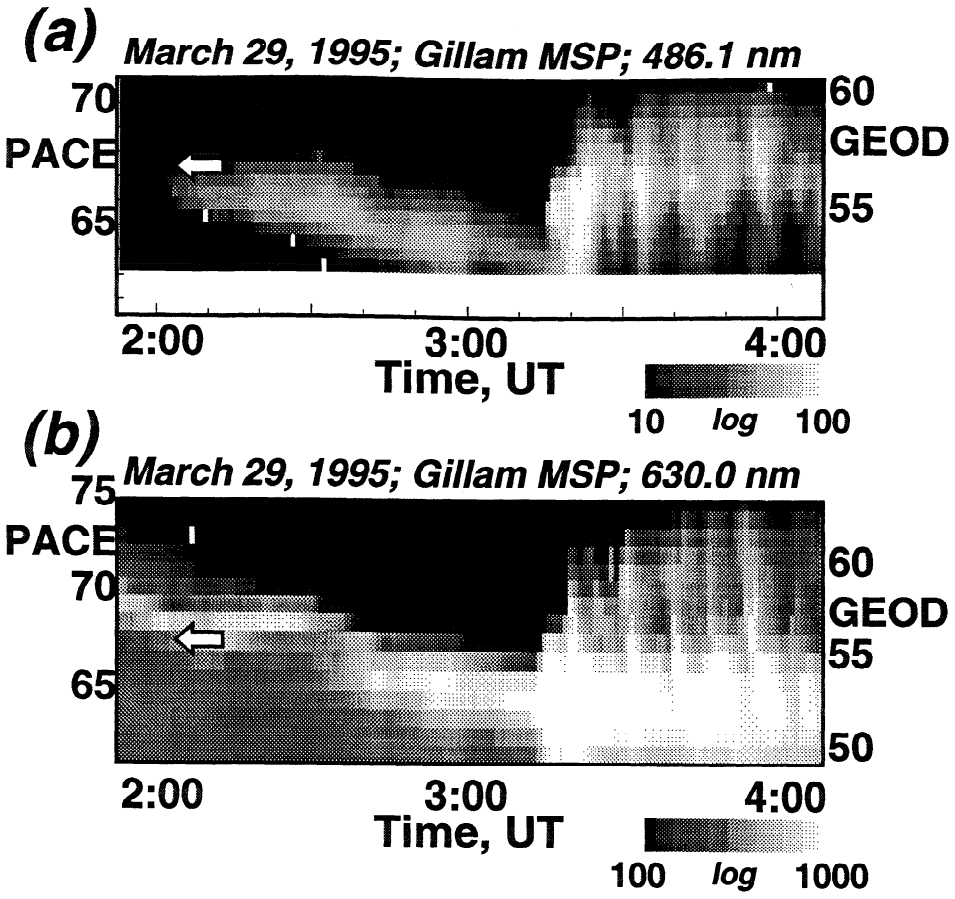

Figure 1. Optical data obtained using the Gillam meridional scanning photometer (MSP) for (a) 486.1-nm and (b) 630.0-nm emissions on March 29, 1995. Arrows point to the position of the initial arc from which the large-scale vortex developed.

those ASI pictures that represent the major stages of vortex evolution. Solid bars show the regions where the Hβ emission was greater than 5 R, which corresponded to ~10% of the Hβ emission maximum values averaged over the entire growth phase, and can be referred as a background luminosity. The longitudinal direction of bars corresponds to the Gillam photometer meridional scan.

For this event the substorm growth phase can be identified using the proton aurora band that intensified and started moving equatorward after 0200 UT. At 0202, the magnitude of the Hβ emission became larger than 10 R; at 0216 - 0218 UT, it established at the level greater than 40 R, and the equatorward motion started at ~0226 UT from 66° latitude PACE (55° GEOD). At 0205 a discrete arc was detected by the Gillam ASI. In Figures 1a and 1b the position of this initial arc is indicated using arrows. As seen from Figure 1, the arc latitude was close to the poleward boundary of the proton aurora region and equatorward boundary of the electron precipitation region. The image of this initial arc is shown in Figure 2 at 0207:07 UT.

For this and subsequent events we provide the initial arc characteristic half thickness, arc-aligned direction with respect to geographic latitudes, and arc-aligned perturbation wavelength, which have been determined as described below. For all values, we have assumed that the arc altitude was 110 km. The total ASI grid is 236 × 236; however, we have disregarded 28 grid points (~1°) at the eastward and westward edges of the image. For every meridional data array, we have found the maximum intensity (meridional maximum magnitude (MMM)), and the arc-aligned direction has been determined as a best fit line for these MMM grid points. In order to find the arc half width, we have subtracted an average value of the complete meridional scan (presumably corresponding to the background intensity), defined the half width as a distance from the MMM to the MMM$\times e^{-1}$ across the arc for every scan, and averaged them through all meridional scans. The arc-aligned perturbation wavelength has been found as a maximum Fourier harmonic of the MMM array. The indicated errors reflect only the standard deviations of data from average values and do not account for possible discrepancies because of the assumed arc altitude. For our purpose, it is more important to find the ratio of the arc width to the arc-aligned wavelength, than their absolute values.

The arc shown in Figure 2 at 0207:07 had a half thickness $\delta = 11 \pm 1$ km. The arc-aligned direction

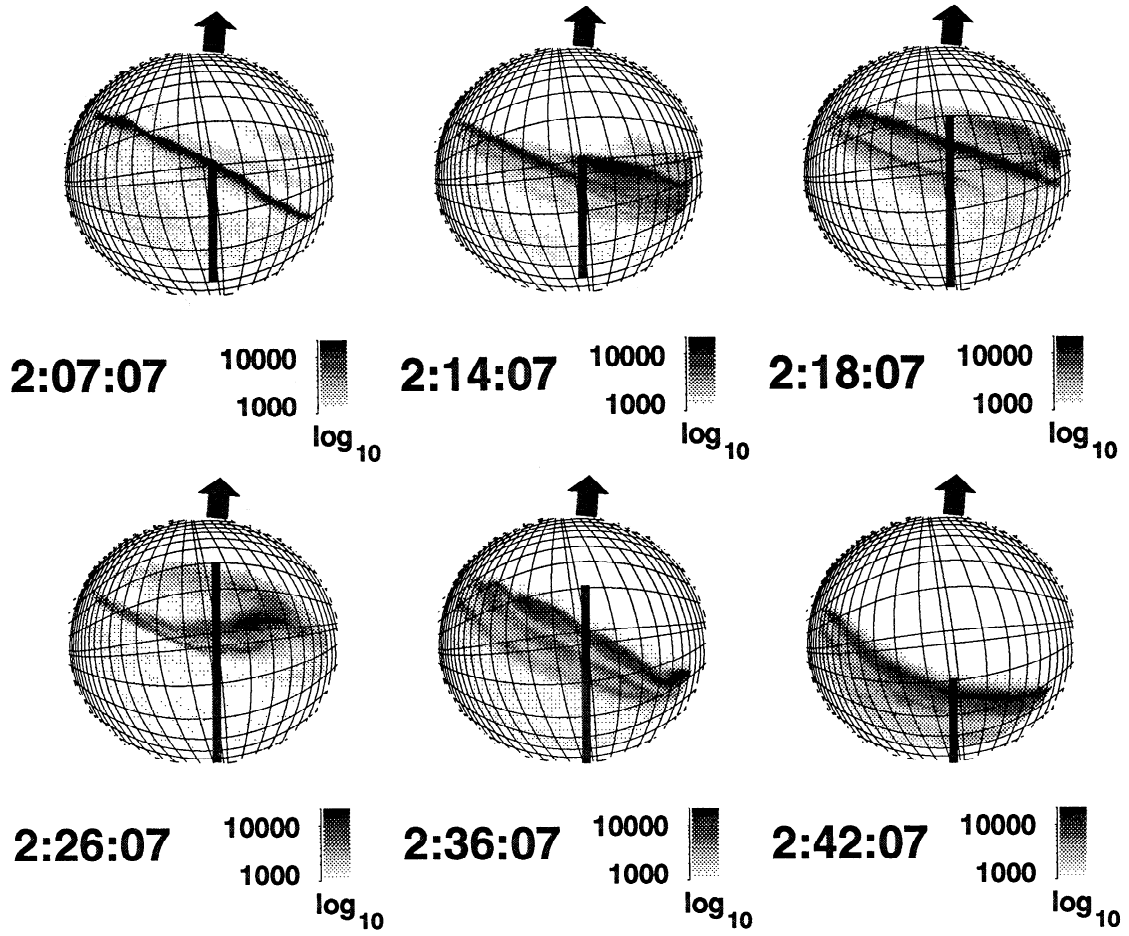

Figure 2. All-sky images showing the main stages of the vortex evolution during the growth phase of March 29, 1995, event. Solid bars indicate the proton aurora region where the intensity of Hβ was larger than 5 R. Solid arrows point the direction toward the magnetic north.

was $21.0° \pm 1.5°$ northeast with respect to the GEOD latitude, which is close to the PACE azimuthal direction. The arc-aligned intensity perturbations had a peak around the harmonic with a wavelength $\lambda = 81 \pm 6$ km. The ratio $2\pi\delta\lambda^{-1}$ is 0.9 ± 0.1.

After 0212 UT the disturbance grew in magnitude and expanded poleward (0214:07 UT and 0218:07 UT images in Figure 2) until it saturated at 0222 UT. As seen from Figure 2, the poleward boundary of the saturated vortex corresponded to the poleward boundary of the proton aurora region. The saturated vortex evolved into a mushroom-like form (shown at 0226:07 UT in Figure 2), which resembles a nonlinear shear flow ballooning vortex saturated at the boundaries of the unstable region [e.g., *Voronkov et al.*, 1997, Figure 11a]. At 0228 - 0229 UT the emissions intensified again. However, the poleward extent of the vortical structure did not increase when compared to the first intensification (it was of the order of 100 km, as seen in Figure 2 for 0236:07 UT). Later, the vortex moved equatorward following the equatorward motion of the proton aurora region and remaining nearby the proton aurora poleward boundary as shown in Figure 2 for 0242:07 UT.

Another example of the large-scale vortex formation was recorded during the pseudo-breakup on April 13, 1996. The Gillam MSP data for 0400 - 0600 UT are presented in Figure 4 which shows that during this period of time there were several auroral intensifications. Below, we shall consider an intensification that started at 0430 UT when the 630.0 nm latitudinal intensity maximum obtained at the Gillam MSP started growing from 280 R, reached its maximum 1689 R at 0442 UT, and then decayed until another intensification started at 0551. The corresponding growth of the 557.7-nm intensity magnitude was from 3126 R at 0430 UT to 14,613 R at 0432 UT and 20,083 R at 0433 UT. We call this event a "pseudo-breakup" following the traditional terminology [*Rostoker*, 1998, and references therein]. However, as was shown by *Rostoker* [1998], there is virtually no difference between onsets of pseudo-breakups and substorm expansive phase. At the later stage, the poleward propagation of the pseudo-breakup active region

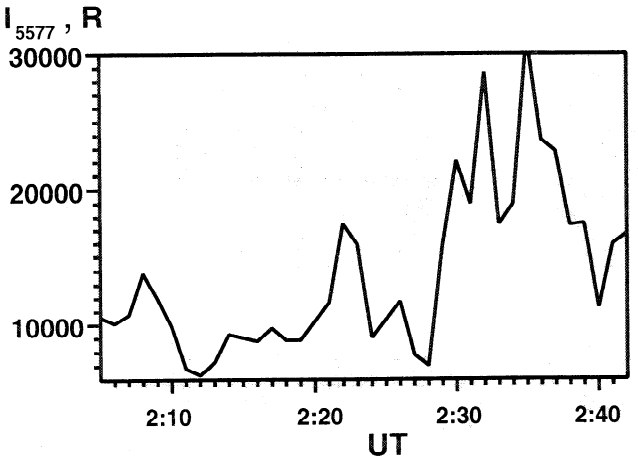

Figure 3. All-sky image intensity for the March 29, 1995, event.

terminates at lower latitudes than during the substorm expansive phase. Thus during the April 13, 1996, 0430-0451 UT, event, the large-scale auroral vortex remained in the ASI field of view for the whole event allowing us to follow its dynamics through the entire event.

A discrete arc with the half width $\delta = 19.6 \pm 0.6$ km intensified and became perturbed at 0429 UT, as shown in Figure 5 for the 0429:06 UT image. The latitudinal alignment of the arc was $9.9° \pm 1.5°$ northeast with respect to the geographic latitude. The arc had an arc-aligned initial perturbation with the wavelength $\lambda = 145 \pm 25$ km. This corresponds to the ratio $2\pi\delta\lambda^{-1} = 0.8 \pm 0.1$. The initial position of this arc is indicated by arrows in Figure 4. As in the previous case, the initial arc latitude corresponded to the poleward boundary of the proton precipitation region and equatorward boundary of the electron precipitation region. The proton precipitation region is shown also in Figure 5 in the same fashion and using the same criteria as for the previous case. At 0430:05 UT the intensity of the vortical structure started growing, as seen from Figure 6 which shows the 557.7-nm all-sky image intensity magnitude. The arc-aligned perturbation initiated the large-scale vortex formation characterized by the growth of the vortex magnitude and its azimuthal expansion. The image intensity grew until 0435 UT and then saturated. The poleward extent of this saturated vortex was close to the poleward boundary of the proton aurora region as shown in Figure 5 for 0436:06 UT.

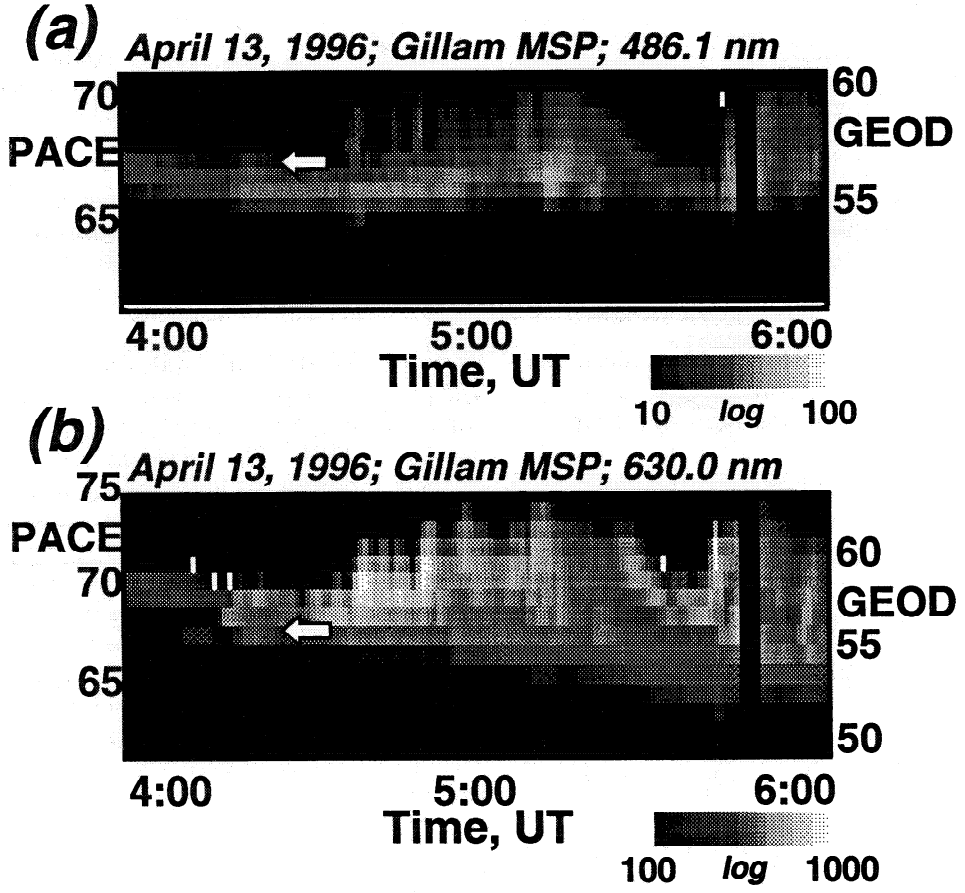

Figure 4. Optical data obtained using the Gillam meridional scanning photometer for (a) 486.1-nm and (b) 630.0-nm emissions on April 13, 1996. Arrows point to the position of the initial arc, as seen in the ASI, from which the large-scale vortex developed during the pseudo-breakup at 0430-0451 UT.

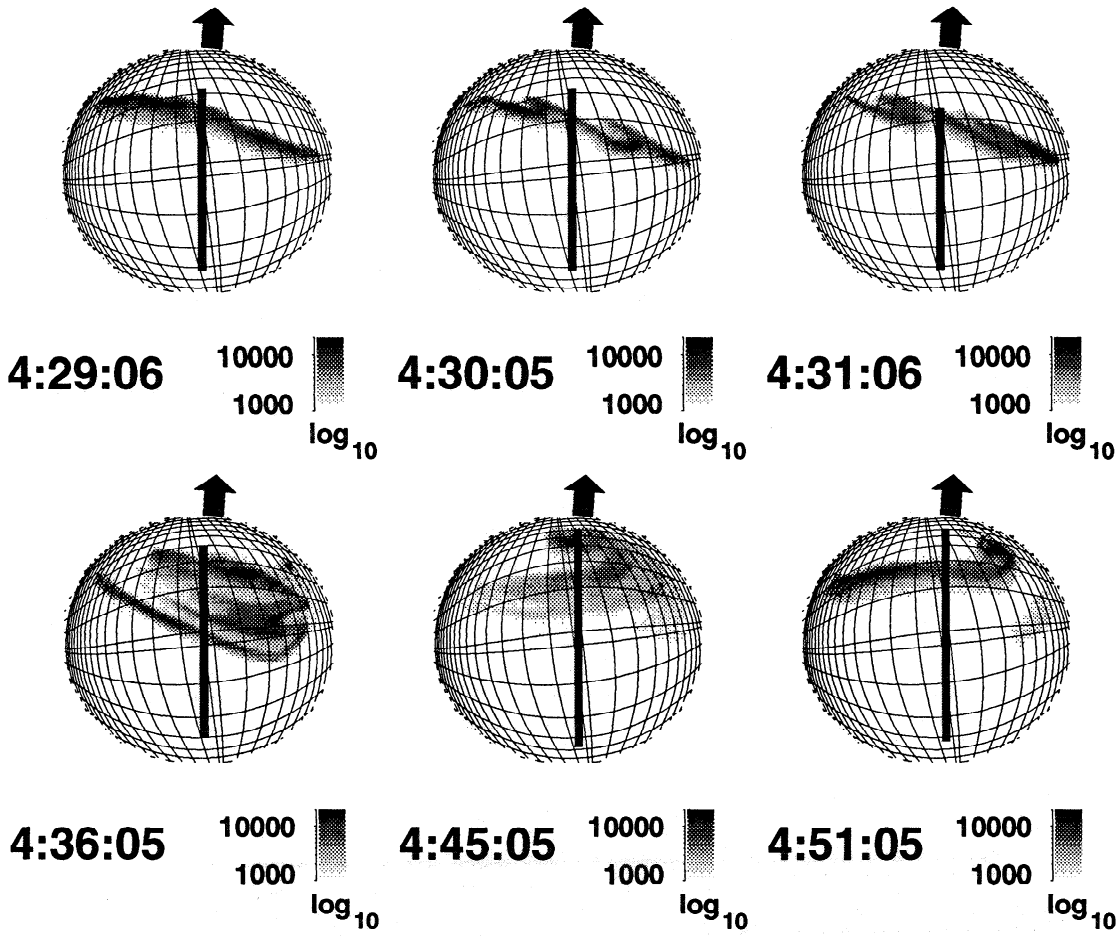

Figure 5. All-sky images showing the main stages of the vortex evolution during the pseudo-breakup at 0430-0451 UT on April 13, 1996. Solid bars indicate the proton aurora region where the intensity of Hβ was larger than 5 R. Solid arrows point the direction toward the magnetic north.

Then this vortex gradually evolved into a mushroom-like structure similar to the previous case. This stage corresponded to the decay of the auroral activity following the pseudo-breakup.

The third example is from a substorm intensification onset on May 11, 1996. This example is illustrated in Figure 7 (Gillam MSP data), Figure 8 (ASI images and the proton precipitation region shown in the same fashion as before), and Figure 9 (magnitudes of all-sky image intensities). The substorm intensification started at 0434 UT. The red line emission intensified from 605 R at 0434 to 962 R at 0441 UT. Even though the increase of the 630.0-nm intensity is comparatively slow and small for this event, we have classified this as a substorm expansive phase onset because of some other signatures characterizing substorms: significant growth of the 557.7-nm intensity magnitude registered by the Gillam MSP (1368 R at 0434 UT and 7143 R at 0441 UT); poleward propagation of the electron precipitation region, as seen in Figure 7b; and poleward propagation of the negative X component magnetic perturbation (positive X is north geographic and close to geomagnetic north) registered by the Churchill meridional line of magnetometers. A preonset arc of magnitude ~2000 R intensified at 0435 UT. The position of the initial arc is marked in Figure 7 using arrows. As in the previous cases, this arc intensified near the poleward boundary of the proton precipitation region and the equatorward boundary of the electron precipitation region. An initial wave-like perturbation is seen in Figure 8 for the 0435:06 UT image. For this image the

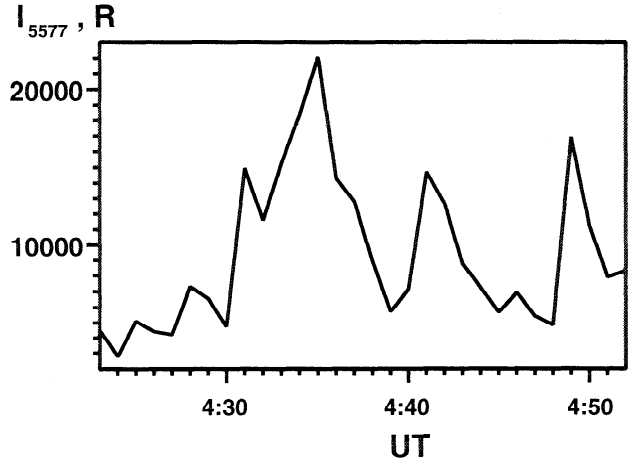

Figure 6. All-sky image intensity for the April 13, 1996, event.

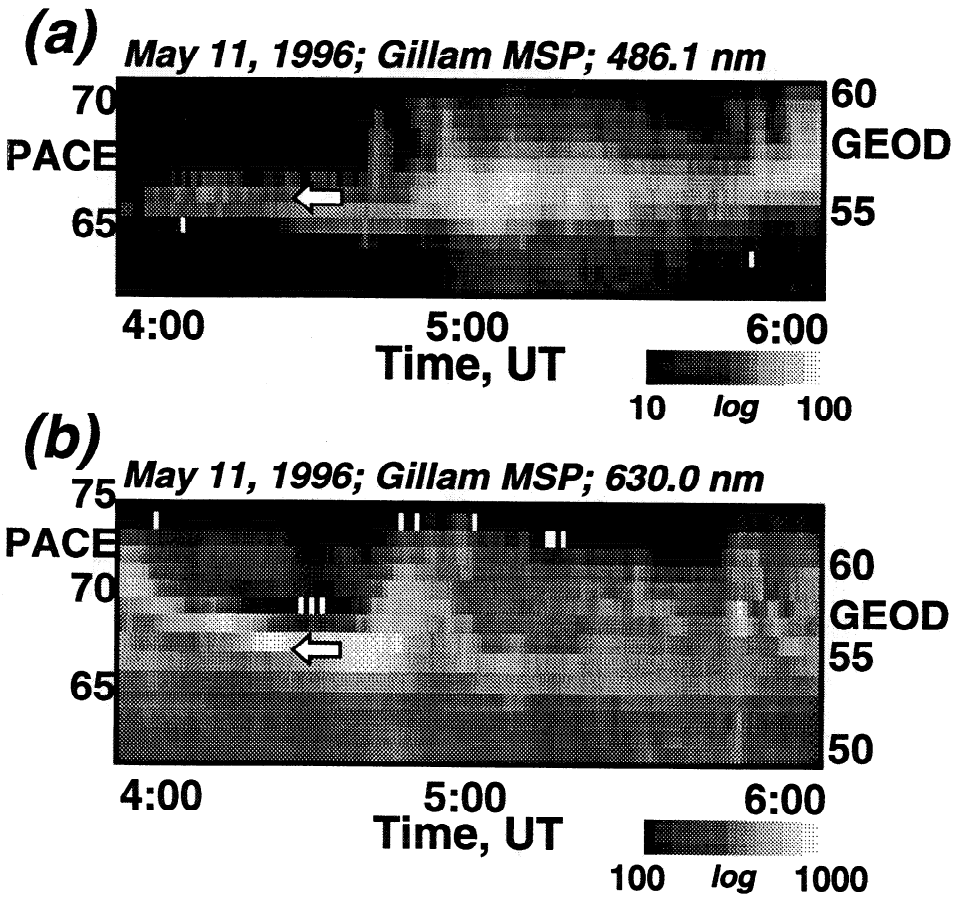

Figure 7. Optical data obtained using the Gillam meridional scanning photometer for (a) 486.1-nm and (b) 630.0-nm emissions on May 11, 1996. Arrows point to the position of the initial arc from which the large-scale vortex developed at times near the substorm expansion phase onset that occurred at 0434 UT.

arc half width was 13.7 ± 0.5 km and the arc alignment was $5.1° \pm 1.5°$ northeast from the geographic latitude. The arc-aligned perturbation had a characteristic wavelength $\lambda = 210 \pm 60$ km. This gives the ratio $2\pi\delta\lambda^{-1} = 0.4 \pm 0.1$. This arc intensity grew in magnitude and the perturbation expanded polewards gradually evolving into a large-scale vortex resembling the vortices described above for two other events. However, the further evolution of this structure can not be traced because, after 0448 UT, the intensity of the emissions decreased either as a consequence of the dissipation of the vortex or its propagation out of field of view.

As suggested by the examples described above, the large-scale vortex formation from an initial discrete arc manifests several common features. In the following paragraph we present the results of the statistical study of the main characteristics of the initial discrete arc and its relative position with respect to the proton aurora. Our statistics are based on all 28 events selected as described above. Errors represent the standard deviation of average numbers obtained for these events.

All events occurred within time interval 0000-0700 UT which corresponds to the evening and near-midnight sectors of the auroral zone. We have identified nine events as breakup accompanied by the substorm expansive phase onset, 15 events as pseudo-breakup, and four large-scale vortices evolved during the growth phase. The vortex formation evolved from a discrete arc embedded in the proton precipitation region. The average intensity of the proton aurora emissions was 37±13 R. The maximum of the proton aurora was observed at the PACE latitude $66.1° \pm 0.7°$, and the proton aurora half thickness was $2.2° \pm 0.6°$. The latitudinal separation of the intensity maxima of the proton aurora and the initial arc was $1.9° \pm 0.8°$. It is important to note that for all events, the initial arc appeared poleward from the proton aurora maximum. The characteristics of the initial discrete arc were as follows: the average half thickness was 23 ± 10 km, the arc was directed at $9° \pm 7°$ northeast with respect to the geographic latitude, and the dominant arc-aligned perturbation had a wavelength $\lambda = 165 \pm 53$ km. The average ratio $2\pi\delta\lambda^{-1}$ equals 0.9 ± 0.2. For further references, some results of this statistical study are accumulated in Table 1.

3. Simulations

In this section, we present results of vortex evolution modeling using parameters and initial conditions that are chosen on the basis of the ground-based observations

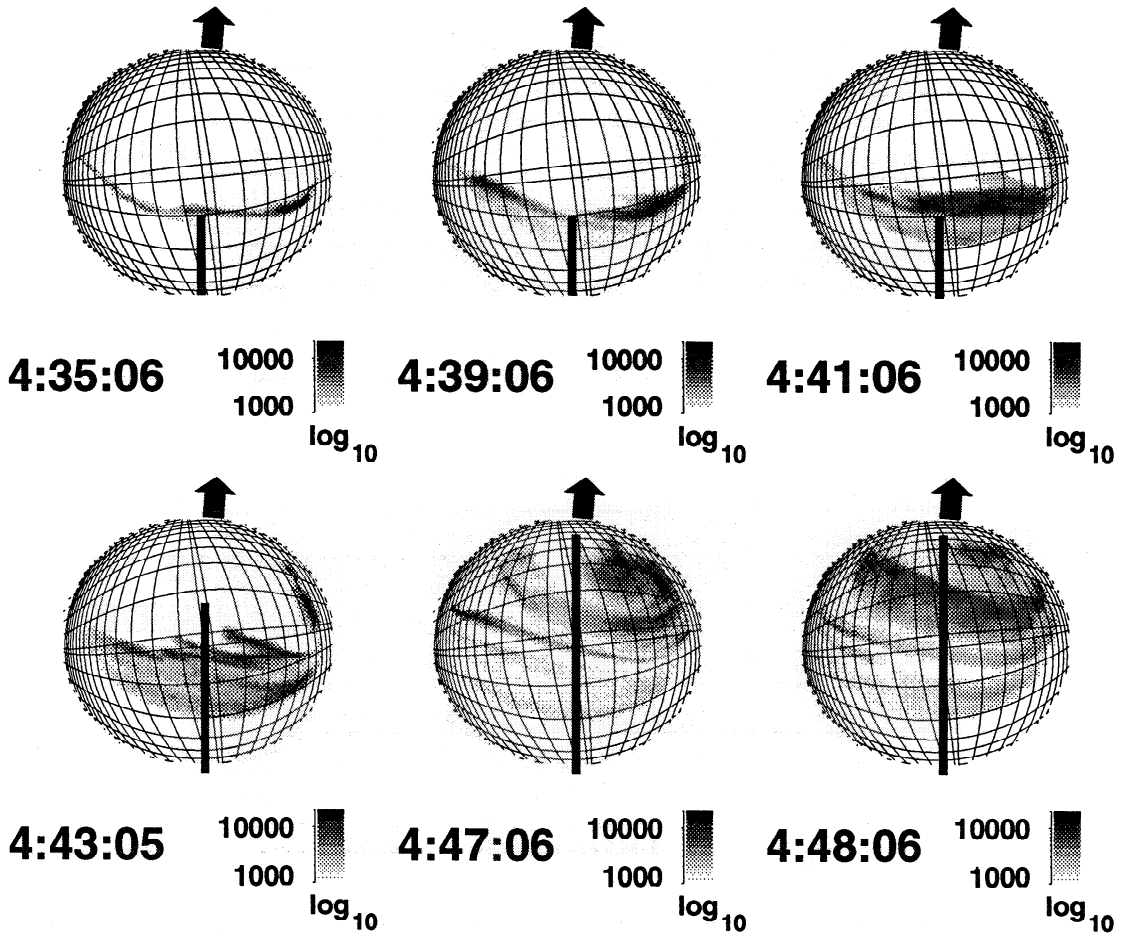

Figure 8. All-sky images showing the main stages of the vortex evolution at and after the substorm expansion phase onset that occurred at 0434 UT on May 11, 1996. Solid bars indicate the proton aurora region where the intensity of Hβ was larger than 5 R. Solid arrows point the direction toward the magnetic north.

described above. Here we discuss several assumptions made for the vortex evolution simulations. In section 4 we present a more detailed discussion of their validity. We have the following assumptions.

1. Ionospheric optical signatures of the large-scale vortex are footprints of the upward field-aligned current driven by the field-aligned gradient of the velocity vorticity $(\nabla \times \mathbf{V})_{\|}$.

2. This vorticity is caused by the shear flow ballooning instability in the near-equatorial plane of the inner plasma sheet.

3. Proton aurora appears on near-dipolar magnetic field lines and it is a footprint of hot proton population at the inner edge of the plasma sheet. As shown by *Samson et al.* [1992], a proton aurora with the magnitude of the order of 30-50 R (based on the Gillam MSP

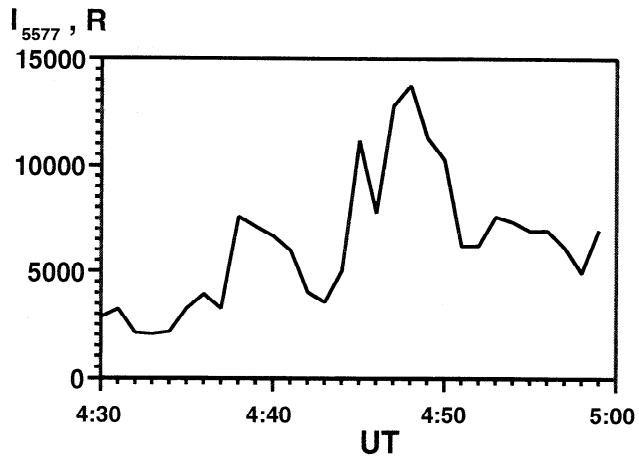

Figure 9. All-sky image intensity for the May 11, 1996, event.

Table 1. Statistical Parameters Characterizing the Proton Aurora Region and the Initial Arc at the Beginning of Vortex Formation

Parameter	Value
Hβ, max	37 ± 13 R at 55.1 °± 0.7°, GEOD, 66.1 °± 0.7°, PACE
I(Arc), max	4700 ± 1600 R at 57.0 °± 0.2°, GEOD, 68.0 °± 0.2°, PACE
δ, km	23±10
λ, km	165±53
$2\pi\delta/\lambda$	0.9±0.2

data) is produced by ~20 keV protons, and the energy of precipitating protons decreases at the poleward edge of the proton aurora. Below we shall use these estimates as well as proton aurora meridional distribution in order to compute the radial pressure profile in the equatorial magnetosphere.

4. Providing that the arc is a footprint of the upward field-aligned current, there is a transverse electric field pointing to the arc. This suggests a shear flow along the arc. Estimating the arc half thickness as ~ 20 km, we also assume the same value for the characteristic transverse scale of the shear flow half thickness, when projected onto the ionospheric level.

5. The characteristic growth time of vortical structures is smaller than the Alfvén transit time from the equatorial plane to the ionosphere and return. This is a reasonable assumption based on the frequencies of field line resonances in the Hβ region [*Samson et al.*, 1996]. In this case we can neglect effects associated with the finite length of magnetic field lines and ionospheric line-tying effects. This justifies the simpler approach of two-dimensional modeling of vortical structures in the equatorial plane. The most important parameter that can be compared with auroral images is the parallel component of vorticity ($(\nabla \times \mathbf{V})_{\|}$), because the field-aligned current above the ionosphere driven by the magnetospheric vortical structure is proportional to the field-aligned gradient of $(\nabla \times \mathbf{V})_{\|}$ [*Voronkov et al.*, 1999].

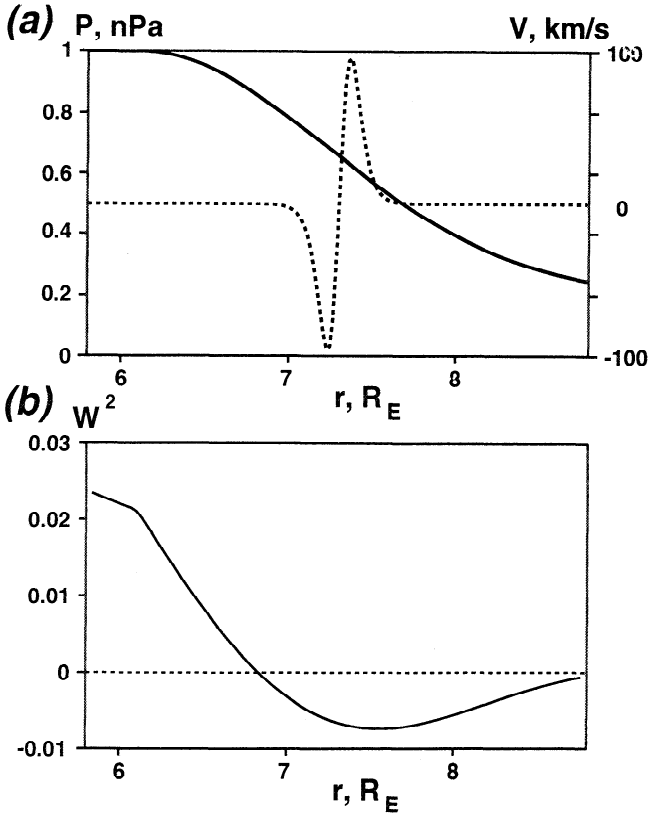

Figure 10. Radial profiles of (a) plasma pressure (solid line) and azimuthal velocity (dashed line, positive eastward) in the equatorial magnetosphere, which are used as initial conditions for the shear flow ballooning vortex modeling, and (b) squared complex frequency of the ballooning instability provided by this plasma pressure profile.

The equatorial pressure profile and azimuthal flow suggested by observations and used as initial conditions for modeling are shown in Figure 10a. For the events considered above, an average maximum of the proton aurora appears at 66.1 that maps at 6.1 R_E in the equatorial plane, providing the field lines are still close to dipolar at these latitudes. The proton aurora band half thickness of 2.2° suggests the earthward pressure gradient with the half thickness of 1.4 R_E. We assumed that the plasma number density is 0.312 cm^{-3} and uniform in the radial direction. This gives a proton energy gradient from 20 keV at 6 R_E to ~4 keV at 8.8 R_E. The total radial extent of the simulation region 5.8-8.8 R_E maps to 65.2°-70.1° latitude in the ionosphere.

The initial auroral arc maximum appeared in average 1.9° poleward from the maximum of the proton aurora. This allows us to assume the shear flow structure at 7.3 R_E in the equatorial plane. The shear flow half thickness δ is chosen 0.1 R_E which corresponds to ~20 km at 110 km altitude for this latitude. The positive direction of the flow was chosen eastward.

The shear flow structure shown in Figure 10a drives an upward field-aligned current sheet (a footprint of the antiearthward gradient of the velocity) embedded into a pair of downward currents that are footprints of the earthward velocity gradient. For the chosen structure and magnitude of the flow, this shear flow in the equatorial plane corresponds to a field-aligned current of the order of 5 μA/m^2 above the highly conductive ionosphere.

For simulations we have used the two-dimensional set of ideal nonlinear magnetohydrodynamic equations in polar coordinates for the equatorial plane of the magnetosphere. Equations are similar to those solved by *Voronkov et al.* [1997]. In this model, the radial momentum equation includes the dipolar magnetic field and the earthward plasma pressure gradient that is in equilibrium with the magnetic curvature force. This force has been represented as $B_0^2/(4\pi R)$, where B_0 is the magnetic field strength and R is its curvature in the equatorial plane. In this model, R is defined by the equilibrium condition that follows from the radial momentum equation and remains constant in time. The complex frequency W of the ballooning instability is defined by

$$W^2 = -\frac{B_0 B_0'}{2\pi R \rho_0} - \frac{2B_0^4}{(4\pi R \rho_0 V_f)^2}, \qquad (1)$$

where $V_f^2 = C_S^2 + V_A^2$, C_S and V_A are acoustic and Alfvén velocities, respectively, and B_0' is the radial derivative of the magnetic field, positive antiearthward. For a case $C_S^2 \ll V_A^2$, this dispersion relation can be easily simplified to

$$W^2 = \frac{2P'}{R\rho_0}. \qquad (2)$$

This equation shows that the earthward gradient of plasma pressure leads to the ballooning unstable con-

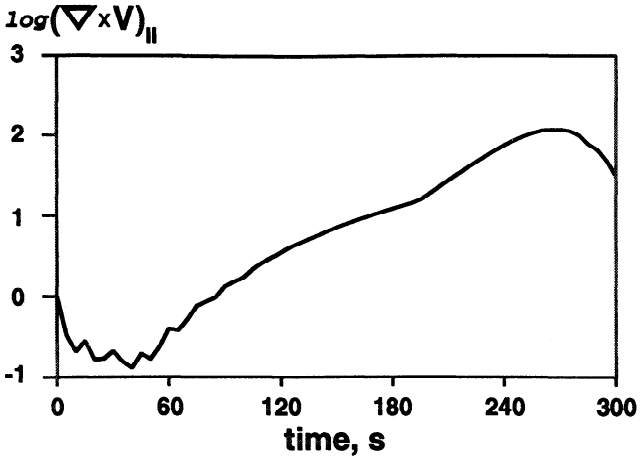

Figure 11. Growth of vorticity magnitude Max($|\nabla \times \mathbf{V}|_{||}$) in the course of the instability. All vorticity magnitudes are normalized by the vorticity magnitude at the start of the simulation.

figuration in the equatorial plane. In the general case of finite $\beta = C_S^2/V_A^2$, equation (1) provides a well-known condition for the ballooning instability

$$P' < \beta P'_B, \tag{3}$$

where $P_B = B^2/(8\pi)$ is the magnetic pressure.

The radial profile of W^2 defined by (1) for the chosen parameters is presented in Figure 10b. The dashed horizontal line shows $W^2 = 0$. Negative values of W^2 correspond to positive growth rates of the instability. At ~6 R_E the dipolar component of the magnetic field is highly stable with respect to ballooning. However, the pressure gradient leads to a significant reduction of the ballooning frequency. Thus at 6.8 R_E this frequency becomes negative which corresponds to the positive growth rate at 6.8-8.8 R_E. At larger radii the configuration is marginally stable.

In order to model the instability from the equilibrium state, we have imposed a small perturbation of the radial velocity on the shear flow structure. This perturbation had magnitude 1 km/s and wavelength λ defined by the ratio $2\pi\delta/\lambda = 1$.

Figure 11 shows the temporal growth of vorticity magnitude (divided by the initial magnitude of the vorticity). After some eigenfunction adjustment lasting for ~1 min, the instability provides a rapid growth of vorticity with an average growth rate 0.0246 s^{-1}, which corresponds to 1 order of magnitude increase in 94 s. This growth is compatible with the growth of vortex intensity obtained using the ASI data as shown in Figures 3, 6, and 9.

In Figure 12 we show different stages of vortex evolution as obtained from our simulations. Four time slices shown in Figure 12 illustrate vorticity spatial distribution in the initial linear growth stage (120 and 180 s), advanced shear flow ballooning instability stage (240 s), and saturation stage (270 s). Note that the positive vorticity in the equatorial plane provides upward field-aligned currents above the ionosphere. The aim of Figure 12 is to show that the shear flow ballooning instability leads to a vortical structure with a radial extent much larger than initial flow thickness. Finally, this vortical structure can become saturated at the ballooning unstable region boundaries, providing a mushroom-like distribution that resembles the saturated vortices observed by the ASI, as in the examples shown in Figures 2 and 5. The radial asymmetry in the vortex propagation is a consequence of the fact that, due to the

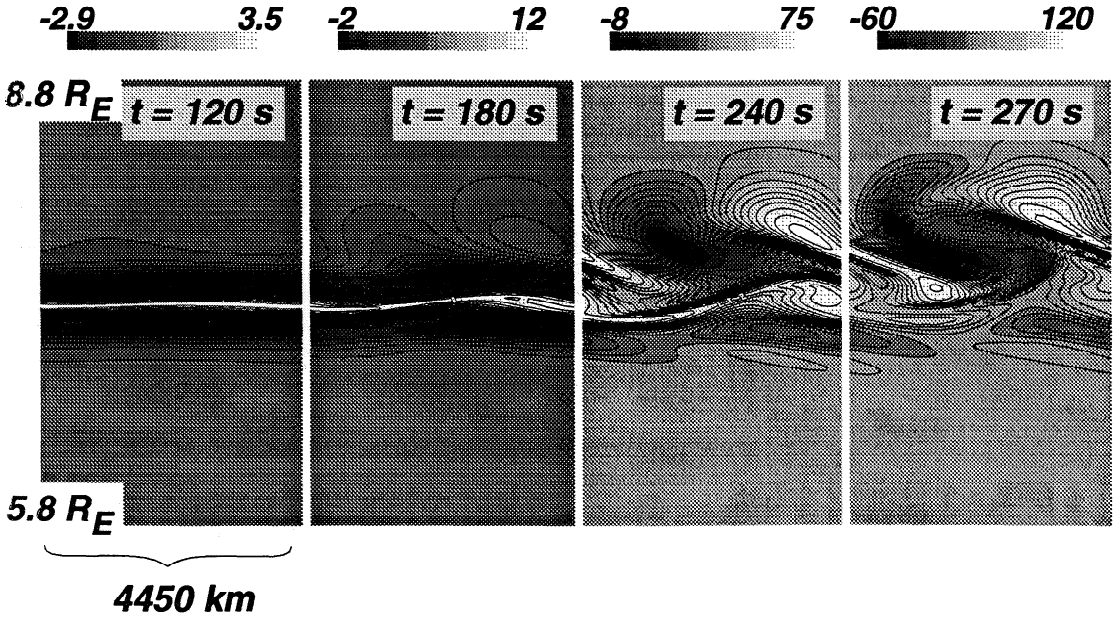

Figure 12. Time slices of vorticity in the equatorial plane. Vertical and horizontal axes correspond to the radial and azimuthal directions. Vorticity magnitudes are normalized as in Figure 11.

background dipolar magnetic field, the configuration is stable Earthward of the initial location of the instability.

4. Discussion

In this paper, we have attempted to identify the origin of large-scale auroral vortices observed by the Gillam ASI. In order to determine the region where and the auroral activity level when vortices evolved, we used the Gillam MSP that has a latitudinal scan of 8° (at 110 km of altitude), more than covering the latitudinal extent of the ASI field of view. We used the database of all-sky images for 1993-1996 years. Amongst all events when large-scale vortices were observed, we have selected only those with growth timescales of the order of a few minutes or larger, and spatial scales of the order of a few hundred kilometers or smaller. In imposing these limitations, we are restricting ourselves to events that can be reasonably studied with the ASI data.

The typical observed dynamics can be summarized as follows. An initial discrete arc with the half thickness of the order of 20 km manifests arc-aligned perturbations (ripples) that grow in amplitude forming folds or curls according to the classification by *Hallinan* [1976]. This stage is followed by broadening of the arc and the longitudinal (radial) expansion of the perturbation, primarily in the poleward direction, that finally forms a vortical structure of the large spatial scale and magnitude. In some cases, we have been able to observe vortex saturation within the ASI field of view. During the saturation stage, the vortex transforms from a spiral-like to a mushroom-like form. This final mushroom-like form implies that the saturation reflects a spatial limitation imposed on the evolution of the instability by proximity to the boundaries of the unstable region.

We have found that large-scale vortices appear near the poleward edge of the proton aurora band. This suggests that the vortices may evolve in the region of adiabatically heated ions at the Earthward edge of the plasma sheet. *Samson et al.* [1992] showed that the proton aurora results from precipitating protons with energies of the order of 20 keV. Assuming that the proton aurora appears on slightly stretched but near-dipolar magnetic field lines, observations by *Samson et al.* [1992] are in agreement with observations of a peak proton energy of ~20-30 keV at ~8 R_E in the magnetotail during preonset times [*Kistler et al.*, 1992]. This suggests that the proton aurora is the ionospheric footprint of the near-Earth energetic proton population and that this region (in the magnetotail) can be a source for unstable pressure gradient (or ballooning) modes. This appears to be in agreement with observations at the geostationary orbit presented by *Roux et al.* [1991] and *Holter et al.* [1995] who identified low-frequency waves during the beginning of substorm expansive phase intensification as ballooning modes.

Another source for the vortex formation is a shear flow that exists along discrete arcs and which is associated with the field-aligned current shear [*Carlson and Kelley*, 1977; *Bruning and Goertz*, 1986; *Haerendel et al.*, 1993, 1996]. This flow can become unstable with respect to the shear flow (or Kelvin-Helmholtz (KH)) instability. Presumably, this instability leads to the formation of curls and folds with characteristic growth time of the order of tens of seconds [*Haerendel et al.*, 1996; *Miura*, 1996; *Trondsen and Cogger*, 1997, 1998]. The KH instability also gives mode selection because different modes have different growth rates. The maximum growth rate occurs for the wavelength $\lambda \sim 2\pi\delta$, where δ is the half width of the shear flow [*Miura and Pritchett*, 1982]. However, the KH instability can not cause large vortex formation as it saturates when the vortex has extracted roughly one half of the flow energy. The corresponding vortex expansion orthogonal to the flow is no larger than roughly one wavelength, which also can not explain the large longitudinal extent of vortices discussed in this paper.

A possible mechanism that can explain the large-scale vortex formation from a narrow arc structure was suggested by *Voronkov et al.* [1997] based on the fact that the KH mode can interact with a ballooning mode. In the case when the KH unstable mode has higher growth rate than ballooning modes, the shear flow vortex grows first and in the nonlinear stage (when the KH instability saturates), it drives a specific ballooning mode. In this sense the shear flow mode plays the role of a mode selector that also provides the large initial perturbation for the ballooning instability. As a result, the hybrid shear flow ballooning vortex can rapidly grow to large amplitude and expand radially to distances much greater than the shear flow thickness enhancing kinetic energy in plasma flows.

The fact that the large vortex formation starts from a discrete arc imbedded in the proton aurora region and that this formation can occur in the region for different levels of auroral activity, as well as the apparent similarity of the dynamics (as recorded by the ASI) with simulations of shear flow ballooning vortices (including temporal and spatial scales) inspired us to compare the ASI data with our simulations. We have shown that the dynamics of large auroral vortices are in qualitative agreement with the results from models of shear flow ballooning. However, there are limitations on our ability to quantitatively compare real and modeled dynamics. The all-sky images employed in this study were obtained at 1-min intervals. Consequently, even for the most slowly evolving vortices, the entire vortex evolution takes place over several frames. As well, we had to reject some events from our study as their evolution took place within 1 min (e.g., for some substorm events). Thus our growth rates must be regarded as estimates not necessarily accurate enough for comparisons with theories.

In section 3 we used a model that is similar to that presented by *Voronkov et al.* [1997]. This model allows us to compute the vortex structure evolution in the central magnetosphere. With some caution this modeling can be compared with optical observations assuming that an auroral optical image is an ionospheric foot-

print of field-aligned current structure (presumably, of the upward field-aligned current) driven by the field-aligned gradient of $(\nabla \times \mathbf{V})_{\|}$ in a similar fashion as excitation of shear Alfvén waves (SAWs). There are several effects that are assumed negligible in this modeling, the most important of which are influence of the magnetic field line curvature on the KH instability, influence of the ionosphere, and effects associated with magnetic field curvature variations in the course of the ballooning instability. In our final paragraphs of this section we discuss the limitations imposed by these assumptions.

The first two assumptions were considered and discussed in detail by *Voronkov et al.* [1999] for three-dimensional shear flow vortex dynamics in the dipolar magnetosphere. Providing the transverse scale of vortices is much smaller than the field line length, which is valid for processes considered in this paper, the reduction of the vortex growth rate imposed by the finite field line length is of the order of the fundamental standing SAW frequency that is of the order of mHz for the L shells corresponding to auroral latitudes. For the events considered in this paper the growth rate can be estimated as 0.01 s^{-1} and higher and therefore this reduction is negligible. The influence of the ionosphere can be summarize as follows [*Miura and Kan,* 1992; *Galinsky and Sonnerup,* 1994; *Miura,* 1996]. For low Pedersen conductivity (of the order of Alfvén conductivity that is typically ~3-5 Sm), the ionosphere absorbs energy which can lead to the vortex growth rate reduction. If the Pedersen conductivity is high, the ionosphere reflects waves leading to vortex decay. However, in both cases the instability in the equatorial magnetosphere is influenced by the ionosphere after the Alfvén transit time that is of the order of 10 min for latitudes of vortices. It is interesting to note that reflection from a highly conducting ionosphere results in periodic growth and decay of vortical structures with a period equal to the standing SAW period [*Voronkov et al.,* 1999]. This may explain the observed oscillations in the all-sky image intensity (Figures 3, 6, and 9) and warrant investigation utilizing three-dimensional simulations and ASI data obtained with greater temporal resolution.

Variations of the magnetic field curvature in the course of the ballooning instability can influence vortex dynamics. As our modeling work does not address this issue, it warrants consideration at this point. Some results of the three-dimensional ballooning instability simulations suggest that in the linear stage this influence is of the order of the ratio of transverse and field-aligned scales of the ballooning unstable region [*Hurricane et al.,* 1997, 1998; *Voronkov,* 1998]. Whenever this ratio is small, the three-dimensional unstable mode evolves in the same fashion as in the model considered above until the mode reaches radial boundaries of the unstable region where it saturates transforming into the mushroom-like form. This appears to be in agreement with those observations that relate to comparatively small longitudinal expansions of vortices. As an example, Figure 13 illustrates an image obtained at the pseudo-breakup saturation stage. This pseudo-breakup occurred on November 29, 1995, at 0551 UT and recovered after 0606 UT. Figure 13 illustrates a clear mushroom-like form at 0606 UT.

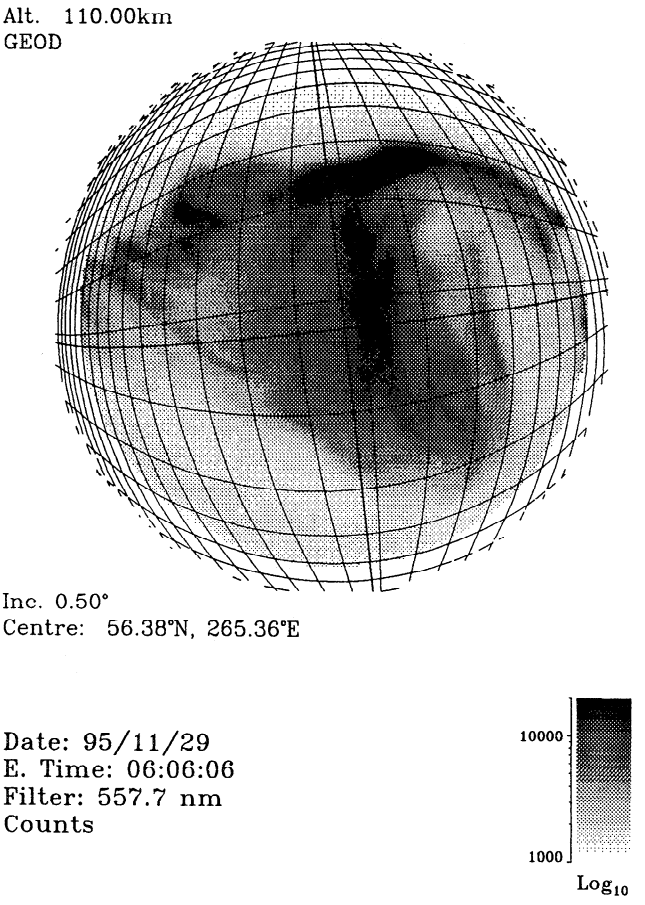

Figure 13. All-sky image during the recovery phase of the pseudo-breakup on November 11, 1995.

For the substorm expansive phase events, vortices seem to disrupt the stabilizing region and expand poleward. For these cases we were able to observe only initial evolution of vortices, whereas further dynamics lie beyond the observational scope of this study. For this reason, we have limited our attempts to simulate vortex dynamics with such a simplified ballooning model. However, there are several recent theoretical models that aim to explain these processes during the substorm expansive phase [*Sundaram and Fairfield,* 1997; *Hurricane et al.,* 1997, 1998; *Bhattacharjee et al.,* 1998; *Cheng and Lui,* 1998; *Lee,* 1998] and further experimental and theoretical studies can be an important step in order to understand expansive phase and substorm triggering mechanisms.

5. Conclusions

We have presented the results of a statistical study of large scale (approximately hundreds of kilometers) auroral vortices that appear in the evening and midnight sectors of the auroral zone and can be observed using

all-sky cameras. These vortices can appear and manifest similar dynamics during different levels and phases of auroral activity such as growth phase, breakup, and pseudo-breakup. Our results lead us to several conclusions regarding the phenomenology of vortex development. At the first stage of vortex evolution, there is an intensification of an arc that is located at the poleward edge of the proton aurora and has a half thickness of ~20 km. The average latitudinal separation between the maximum intensity of the proton aurora and this arc was found to be ~2° due poleward. This arc manifests a small arc-aligned perturbation with a ~160 km wavelength, providing the average ratio $2\pi\delta/\lambda \sim 1$. This perturbation grew in magnitude and expanded poleward. During growth phase and pseudo-breakup, we have observed the saturation stage of these vortices. At this stage the vortex transforms into a mushroom-like form presumably matching the boundaries of the unstable region. Utilizing recent models of the shear flow and ballooning instabilities by *Voronkov et al.* [1997 and 1999] and using initial condition parameters suggested by observations, we have shown that model vortices that appear due to the coupling of the shear flow and ballooning unstable modes are in good agreement with observed large-scale vortices. The model reproduces the growth of the initial perturbation, its tailward (in the equatorial magnetosphere at 6-9 R_E) expansion, and nonlinear saturation with temporal and spatial scales that are close to observations.

Acknowledgments. Karen Apps and Erena Friedrich provided invaluable assistance with the CANOPUS software. We used Greg Baker's statistical survey of the CANOPUS ASI data set as a road map to help us identify interesting events in an expedient manner. As well, we appreciate the efforts of Leroy Cogger who is the Principle Investigator for the CANOPUS ASI. This research was supported by the Natural Sciences and Engineering Research Council of Canada (NSERC) through the operating grant to John Samson. The CANOPUS array is a ground-based facility funded and operated by the Canadian Space Agency.

Janet G. Luhmann thanks the referees for their assistance in evaluating this paper.

References

Akasofu, S.-I., *Physics of Magnetospheric Substorms,* 599 pp., D. Reidel, Norwell, Mass., 1977.

Baker, K. B., and S. Wing, A new magnetic coordinate system for conjugate studies at high latitude, *J. Geophys. Res., 94,* 9139, 1989.

Bhattacharjee, A., Z. W. Ma, and X. Wang, Ballooning instability of a thin current sheet in the high-Lundquist-number magnetotail, *Geophys. Res. Lett., 25,* 861, 1998.

Blanchard, G. T., L. R. Lyons, and J. C. Samson, Accuracy of using 6300 Å auroral emission to identify the magnetic separatrix on the nightside of Earth, *J. Geophys. Res., 102,* 9697, 1997.

Bruning, K., and C. K. Goertz, Dynamics of a discrete auroral arc, *J. Geophys. Res., 91,* 7057, 1986.

Carlson, C. W., and M. C. Kelley, Observation and interpretation of particle and electric field measurements inside and adjacent to an active auroral arc, *J. Geophys. Res., 82,* 2349, 1977.

Cheng, C. Z., and A. T. Y. Lui, Kinetic ballooning instability for substorm onset and current disruption observed by AMPTE/CCE, *Geophys. Res. Lett., 25,* 4091, 1998.

Elphinstone, R. D., et al., Observations in the vicinity of substorm onset: Implications for the substorm process, *J. Geophys. Res., 100,* 7937, 1995.

Frank, L. A., J. B. Sigwarth, and W. R. Paterson, High-resolution global images of Earth's auroras during substorms, in *SUBSTORM-4, International Conference on Substorms-4, Lake Hamana, Japan: March 9-13, 1998,* p. 3, Terra Sci., Tokyo, 1998.

Galinsky, V. L., and B. U. O. Sonnerup, Dynamics of shear velocity layer with bent magnetic field lines, *Geophys. Res. Lett., 21,* 2247, 1994.

Haerendel, G., S. Buchert, C. La Hoz, B. Raaf, and E. Rieger, On the proper motion of auroral arcs, *J. Geophys. Res, 98,* 6087, 1993.

Haerendel, G., B. U. Olipitz, S. Buchert, O. H. Bauer, E. Rieger, and C. La Hoz, Optical and radar observations of auroral arcs with emphasis on small-scale structures, *J. Atmos. Terr. Phys., 58,* 71, 1996.

Hallinan, T. J., Auroral spirals, 2, Theory, *J. Geophys. Res, 81,* 3959, 1976.

Holter, O., C. Altman, A. Roux, S. Perraut, A. Pedersen, H. Pecseli, B. Lybekk, J. Trulsen, A. Korth, and G. Kremser, Characterization of low frequency oscillations at substorm breakup, *J. Geophys. Res., 100,* 19,109, 1995.

Hurricane, O. A., B. H. Fong, and S. C. Cowley, Nonlinear magnetohydrodynamic detonation, 1, *Phys. Plasmas, 4*(10), 3565, 1997.

Hurricane, O. A., B. H. Fong, S. C. Cowley, F. V. Coroniti, C. F. Kennel, and R. Pellat, Substorm detonation - the unification of substorm trigger mechanisms, in *SUBSTORM-4, International Conference on Substorms-4, Lake Hamana, Japan: March 9-13, 1998,* p. 373, Terra Sci., Tokyo, 1998.

Kelley, M. C., Intense sheared flow as the origin of large-scale undulations of the edge of the diffuse aurora, *J. Geophys. Res., 91,* 3225, 1986.

Kidd, S. R., and G. Rostoker, Distribution of auroral surges in the evening sector, *J. Geophys. Res., 96,* 5697, 1991.

Kistler, L. M., E. Möbius, W. Baumjohann, G. Paschmann, and D. C. Hamilton, Pressure changes in the plasma sheet during substorm injections, *J. Geophys. Res., 97,* 2973, 1992.

Lee, D.-Y., Ballooning instability in the tail plasma sheet, *Geophys. Res. Lett., 25,* 4095, 1998.

Miura, A., Stabilization of the Kelvin-Helmholtz instability by the transverse magnetic field in the magnetosphere-ionosphere coupling system, *Geophys. Res. Lett., 23,* 761, 1996.

Miura, A., and J. R. Kan, Line-tying effects on the Kelvin-Helmholtz instability, *Geophys. Res. Lett., 19,* 1611, 1992.

Miura, A., and P. L. Pritchett, Nonlocal stability analysis of the MHD Kelvin-Helmholtz instability in a compressible plasma, *J. Geophys. Res., 87,* 7431, 1982.

Murphree, J. S., and M. L. Johnson, Clues to plasma processes based on Freja UV observations, *Adv. Space Res., 18,* 95, 1996.

Rankin, R., B. G. Harrold, J. C. Samson, and P. Frycz, The nonlinear evolution of field line resonances in the Earth's magnetosphere, *J. Geophys. Res., 98,* 5839, 1993.

Rostoker, G., On the place of the pseudo-breakup in a magnetospheric substorm, *Geophys. Res. Lett., 25,* 217, 1998.

Roux, A., S. Perraut, P. Robert, A. Morane, A. Pedersen, A. Korth, G. Kremser, B. Aparicio, D. Rodgers, and R. Pellinen, Plasma sheet instability related to the westward traveling surge, *J. Geophys. Res., 96,* 17697, 1991.

Samson, J. C., L. R. Lyons, P. T. Newell, F. Creutzberg, and B. Xu, Proton aurora and substorm intensifications, *Geophys. Res. Lett., 19,* 2167, 1992.

Samson, J. C., L. L. Cogger, and Q. Pao, Observations of field line resonances, auroral arcs, and auroral vortex structures, *J. Geophys. Res., 101,* 17373, 1996.

Samson, J. C., R. Rankin, and I. Voronkov, Field line resonances, auroral arcs, and substorm intensifications, in *Geospace Mass and Energy Flow: Results From the International Solar-Terrestrial Physics Program, Geophys. Monogr. Ser.,* vol. 104, edited by J. L. Horwitz, D. L. Galagher, and W. K. Peterson, p. 161, AGU, Washington, D. C., 1998.

Steen, Å., and P. N. Collis, High time-resolution imaging of auroral arc deformation at substorm onset, *Planet. Space Sci., 36,* 715, 1988.

Sundaram, A. K., and D. H. Fairfield, Stability of resistive MHD tearing and ballooning modes in the tail current sheet, *J. Geophys. Res., 102,* 19,913, 1997.

Trondsen, T. S., and L. L. Cogger, High-resolution television observations of black aurora, *J. Geophys. Res., 102,* 363, 1997.

Trondsen, T. S., and L. L. Cogger, A survey of small-scale spatially periodic distortions of auroral forms, *J. Geophys. Res., 103,* 9405, 1998.

Voronkov, I., Shear Alfvén waves and shear flow instabilities in the Earth's magnetosphere, Ph.D. thesis, 181 pp., Univ. of Alberta, Edmonton, Alberta, 1998.

Voronkov, I., R. Rankin, P. Frycz, V. T. Tikhonchuk, and J. C. Samson, Coupling of shear flow and pressure gradient instabilities, *J. Geophys. Res., 102,* 9639, 1997.

Voronkov, I., R. Rankin, J. C. Samson, and V. T. Tikhonchuk, Shear flow instability in the dipolar magnetosphere, *J. Geophys. Res., 104,* 17,323, 1999.

E. F. Donovan and B. J. Jackel, Department of Physics and Astronomy, University of Calgary, Calgary, Alberta, Canada, T2N 1N4. (donovan@phys.ucalgary.ca; jackel@phys.ucalgary.ca)

J. C. Samson and I. Voronkov, Department of Physics, University of Alberta, Edmonton, Alberta, Canada, T6G 2J1. (samson@space.ualberta.ca; igor@space.ualberta.ca)

(Received December 2, 1999; revised February 18, 2000; accepted February 18, 2000.)